

Instant trachea reconstruction using 3D-bioprinted C-shape biomimetic trachea based on tissue-specific matrix hydrogels

Yuyan Sun^{a,b,e,1}, Yingying Huo^{a,e,1}, Xinyue Ran^{a,b,e,1}, Hongying Chen^d, Qingqing Pan^d, Yujie Chen^f, Ying Zhang^a, Wenjie Ren^d, Xiaoyun Wang^{c,**}, Guangdong Zhou^{a,b,d,e,*}, Yujie Hua^{a,d,e,***}

^a Department of Plastic and Reconstructive Surgery, Shanghai Ninth People's Hospital, Shanghai Jiao Tong University School of Medicine, Shanghai Key Laboratory of Tissue Engineering, Shanghai, 200011, PR China

^b Research Institute of Plastic Surgery, Weifang Medical University, Weifang, Shandong, 261053, PR China

^c Department of Plastic Surgery, Tongren Hospital Shanghai Jiao Tong University School of Medicine, Shanghai, 200050, PR China

^d Institute of Regenerative Medicine and Orthopedics, Institutes of Health Central Plain, Xinxiang Medical University, Xinxiang, Henan, 453003, PR China

^e National Tissue Engineering Center of China, Shanghai, 200241, PR China

^f Morphology and Spatial Multi-omics Technology Platform, Shanghai Institute of Nutrition and Health, Chinese Academy of Sciences, Shanghai, 200031, PR China

ARTICLE INFO

Keywords:

Trachea reconstruction
3D-bioprinting
Hydrogels
Biomimetic architecture

ABSTRACT

Currently, 3D-bioprinting technique has emerged as a promising strategy to offer native-like tracheal substitutes for segmental trachea reconstruction. However, there has been very limited breakthrough in tracheal repair using 3D-bioprinted biomimetic trachea owing to the lack of ideal bioinks, the requirement for precise structural biomimicking, and the complexity of multi-step surgical procedures by mean of intramuscular pre-implantation. Herein, we propose a one-step surgical technique, namely direct end-to-end anastomosis using C-shape 3D-bioprinted biomimetic trachea, for segmental trachea defect repair. First, two types of tissue-specific matrix hydrogels were exploited to provide mechanical and biological microenvironment conducive to the specific growth ways of cartilage and fibrous tissue respectively. In contrast to our previous O-shape tracheal design, the tubular structure of alternating C-shape cartilage rings and connecting vascularized-fibrous-tissue rings was meticulously designed for rapid 3D-bioprinting of tracheal constructs with optimal printing paths and models. Furthermore, *in vivo* trachea regeneration in nude mice showed satisfactory mechanical adaptability and efficient physiological regeneration. Finally, *in situ* segmental trachea reconstruction by direct end-to-end anastomosis in rabbits was successfully achieved using 3D-bioprinted C-shape biomimetic trachea. This study demonstrates the potential of advanced 3D-bioprinting for instant and efficient repair of segmental trachea defects.

1. Introduction

Segmental trachea reconstruction remains a significant challenge in the clinic owing to the lack of ideal tracheal substitutes [1–3]. Emerging tissue engineering that combines seed cells with biocompatible scaffolds is a promising strategy to construct engineered biomimetic trachea with

native-like architecture [4–7]. As known, the native trachea displays a complex and heterogeneous structure of alternating C-shape cartilage (C-C) rings and connecting vascularized-fibrous-tissue (VF) rings as well as an intraluminal epithelium layer [8]. Currently, multicellular three-dimensional (3D) bioprinting technique has presented as an attractive strategy to construct engineered tissues or organs with

Peer review under responsibility of KeAi Communications Co., Ltd.

* Corresponding author. Department of Plastic and Reconstructive Surgery, Shanghai Ninth People's Hospital, Shanghai Jiao Tong University School of Medicine, Shanghai Key Laboratory of Tissue Engineering, Shanghai, 200011, PR China.

** Corresponding author.

*** Corresponding author. Department of Plastic and Reconstructive Surgery, Shanghai Ninth People's Hospital, Shanghai Jiao Tong University School of Medicine, Shanghai Key Laboratory of Tissue Engineering, Shanghai, 200011, PR China.

E-mail addresses: gaokongliuyun@126.com (X. Wang), guangdongzhou@126.com (G. Zhou), yujiehua@shsmu.edu.cn (Y. Hua).

¹ These authors contributed equally: Yuyan Sun, Yingying Huo, Xinyue Ran.

<https://doi.org/10.1016/j.bioactmat.2023.09.011>

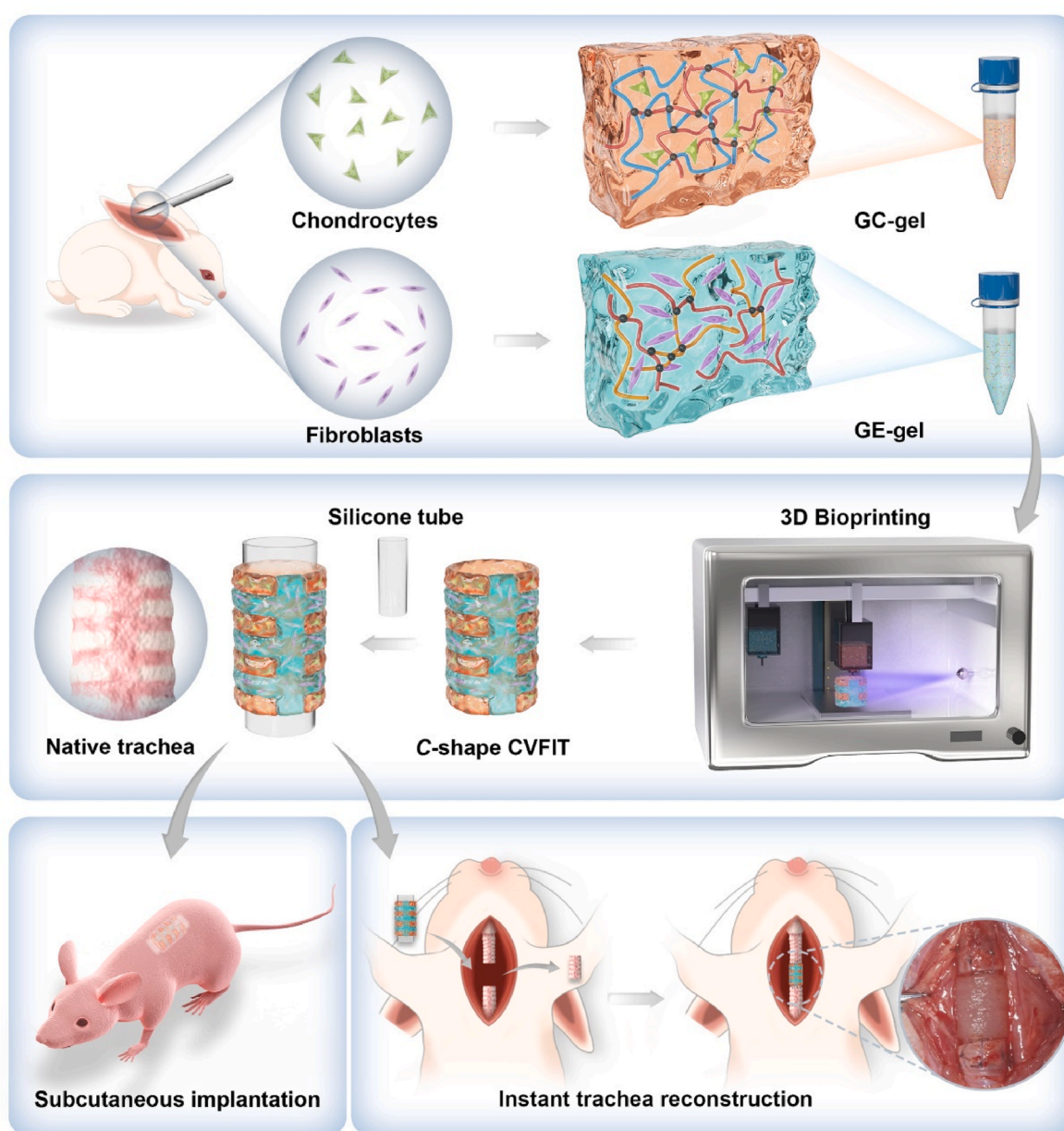
Received 14 July 2023; Received in revised form 17 September 2023; Accepted 18 September 2023

2452-199X/© 2023 The Authors. Publishing services by Elsevier B.V. on behalf of KeAi Communications Co. Ltd. This is an open access article under the CC BY-NC-ND license (<http://creativecommons.org/licenses/by-nc-nd/4.0/>).

heterogeneous architecture, such as the heart, lung, ear, and trachea [9–13]. Our group has recently developed a feasible strategy, namely 3D-bioprinting cartilage-vascularized fibrous tissue-integrated trachea (CVFIT), for segmental trachea defect repair [14]. However, previous research has mainly focused on 3D-bioprinting O-shape biomimetic CVFIT, which lacks the C-shape structure of C rings and the interconnection of VF rings [15–17]. Except the inherent mechanical functions of compressive resistance and lateral flexibility dependent on the alternating stiff-to-soft tissue architecture, the C-shape structure dissipates anisotropic forces to allow physiologically dynamic movements of the trachea [18,19]. Additionally, it is imperative to build a complete vascular network throughout the whole cartilaginous structure for the efficient transport of blood and nutrients [20,21]. Therefore, there is an urgent need to precisely mimic the tissue architecture of C-shape biomimetic trachea with alternating C-C and VF rings based on 3D-bioprinting technique.

In addition to the biomimetic structural design, another essential

consideration is the efficiency of the tracheal repair mode. Generally, *in situ* repair of segmental trachea defects using engineered biomimetic trachea is based on the classical two-step method, namely intramuscular pre-implantation and then end-to-end anastomosis by pedicled muscle transplantation, which is an intricate and time-consuming operation [22–24]. Of course, direct end-to-end anastomosis would avoid secondary surgery, but there is still limited breakthrough due to the comprehensive difficulties of 3D-bioprinting technique. To realize instant and efficient trachea reconstruction using 3D-bioprinted biomimetic trachea, the following are essential requirements: *i*) easily prepared bioinks that beneficial for tissue-specific regeneration; *ii*) simplified printing paths and 3D models to shorten the manufacturing time; *iii*) 3D-bioprinted biomimetic trachea with sufficient mechanical strength and structural stability; and *iv*) improvement of end-to-end anastomosis to replace the traditional two-step surgery. Among these basic requirements, the availability of tissue-specific bioinks is pre-requisite for the rapid and efficient 3D-bioprinting of tracheal



Scheme 1. Schematic illustration of instant trachea reconstruction using 3D-bioprinted C-shape cartilage-vascularized fibrous tissue-integrated trachea based on tissue-specific matrix hydrogels.

constructs. In our previous studies, photocrosslinkable matrix gels were meticulously designed to mimic the main components of extracellular matrix (ECM) by combining both proteoglycans and glycosaminoglycans [25–29]. For example, gelatin methacryloyl (GelMA) hydrogels together with cartilage or dermal acellular matrices can provide satisfactory tissue-specific microenvironments, but the complex composition and potential of biosafety concerns hinder further clinical translation of these hydrogels [30,31]. Some natural materials (e.g., hyaluronic acid, chondroitin sulfate, and elastin) displaying unique biological functions can also be prepared as tissue-specific matrix gels [32–34]. Despite the above initiatives, instant and efficient trachea reconstruction by 3D-bioprinting technique remains elusive.

Herein, we report a novel strategy for *in situ* trachea reconstruction through direct end-to-end anastomosis using 3D-bioprinted C-shape biomimetic trachea (Scheme 1). Two tissue-specific matrix hydrogels were conveniently prepared by hybrid photocrosslinking strategy that combining printable GelMA with chondroitin sulfate methacryloyl (CSMA) as cartilage-specific matrix gels, while elastin methacryloyl (ElaMA) as fibrous tissue-specific matrix gels. The tubular architecture of alternating C-C and VF rings was rapidly 3D-bioprinted by simplifying the printing paths and 3D models, which enabled precise mimicking of the physiological architecture and functions of the native trachea. Furthermore, the feasibility of trachea regeneration with mechanical and physiological functions was investigated by subcutaneous implantation of both O-shape and C-shape biomimetic CVFIT. Finally, *in situ* trachea reconstruction was evaluated by direct end-to-end anastomosis using 3D-bioprinted C-shape biomimetic trachea. This study demonstrates a promising alternative strategy for segmental trachea defect repair by 3D-bioprinting technique.

2. Materials and methods

2.1. Materials and animals

In this study, gelatin, chondroitin sulfate, elastin, methacrylic anhydride, sodium hydroxide, culture medium, trypsin, collagenase, and lithium phenyl-2,4,6-trimethylbenzoylphosphinate (LAP) were purchased from Sigma-Aldrich. All the other chemicals were reagent grade and deionized water was used. Both nude mice and New Zealand white rabbits were purchased from Shanghai Yunde Experimental Animal Raising Farm. All protocols for experimental in animals were approved by the Animal Care and Experimental Committee of Shanghai Jiao Tong University School of Medicine (SH9H-2021-A655-SB).

2.2. Preparation of matrix hydrogels

First, GelMA, CSMA, and ElaMA polymers were respectively synthesized through methacrylation reaction and determined by ^1H NMR spectra according to the previous protocols [35–37]. Then, GelMA, CSMA, and ElaMA polymers were dissolved in Dulbecco PBS (D-PBS, pH 7.4) and mixed according to different constitutes for preparing GC-gel and GE-gel respectively. The above hydrogel samples were subjected to different measurements following light irradiation (365-nm LED, 20 mW cm^{-2}) for 30 s. And the dried hydrogel samples were dehydrated by freeze drying and analyzed by scanning electron microscopy (SEM, Philips XL-30). The hydrogel composition in this study were listed as follows: **G-gel**: 5% w/v GelMA; **GC-gel**: 5% w/v GelMA/1% w/v CSMA; **GE-gel**: 5% w/v GelMA/1% w/v ElaMA. (w/v: weight/volume).

2.3. Rheological measurement

Dynamic rheology experiments were performed on HAAKE MARS III photorheometer with parallel-plate (P20 TiL, 20 mm diameter) geometry and 365-nm (20 mW cm^{-2}) light source at 25 °C. Time sweep oscillatory tests were performed at a 10% strain (CD mode), 1 Hz frequency, and a 0.5 mm gap for 60 s. The gel point was determined as the

time when the storage modulus (G') surpassed the loss modulus (G''). The final storage modulus was determined as the storage modulus (G') reaching to the complete gelation. Temperature-sweep oscillatory tests were performed at 10% strain (CD mode) and 1 Hz frequency parameters from 50 to 4 °C. The sol-to-gel transition point was determined as the time when the storage modulus (G') surpassed the loss modulus (G'').

2.4. Swelling and degradation tests

The cylindrical hydrogel samples (diameter = 8 mm; height = 3 mm) prepared according to the above protocols were recorded as the initial weight (W_0). For swelling tests, hydrogels were fully immersed in D-PBS solution (pH = 7.4) for 24 h until complete swelling. When the mass of these hydrogels was constant, the values were recorded as the wet weight (W_t). The swelling ratio (%) was calculated according to Equation (1):

$$\text{Swelling ratio (\%)} = W_t/W_0 \times 100\% \quad (1)$$

For enzyme-mediated degradation tests, the initial weight (W_0) of hydrogels after complete swelling was firstly recorded. Then, hydrogels were incubated in D-PBS (pH = 7.4) containing 20 U mL^{-1} hyaluronidase and 20 U mL^{-1} collagenase for 6-h observation at 37 °C. At each time point, these samples were carefully collected, gently blotted with filter paper to remove excess water on the surfaces, and recorded as the residual weights (W_t). The degradation ratio (%) was calculated according to Equation (2):

$$\text{Degradation ratio (\%)} = (W_0 - W_t)/W_0 \times 100\% \quad (2)$$

2.5. Observation of interfacial integration

For the visualization of interfacial region, GC-gel hydrogels were stained with rhodamine (red) and GE-gel hydrogels were stained with Aniline blue (blue) respectively. Confocal laser scanning microscopy (CLSM; Leica TCS SP8 STED 3X) was used to directly observe the interfacial integration between GC-gel and GE-gel hydrogels.

2.6. Mechanical measurement

For mechanical tests, hydrogel samples were prepared as cylindrical shape (8 mm in diameter and 3 mm height). The compression tests were carried out using a mechanical analyzer (Instron-5542) with a capacity of 500 N. The as-prepared hydrogels were subjected to compression tests after complete gelation upon light irradiation (365-nm LED, 20 mW cm^{-2}) for 30 s. For compression tests, the testing speed was set at 1 mm min^{-1} up to a maximum of 95% of the deformation. The compressive modulus was calculated as the slope of the linear region (35–55% strain). The cycle compression tests were conducted under a continuous planar unconfined strain rate of 1 mm min^{-1} up to a maximum of 60% of the deformation.

2.7. Finite element analyses

The finite element analyses were compared between 3D-bioprinted O-shape and C-shape biomimetic trachea. The size of regenerated trachea was listed as follows: 11 mm in height; 8 mm in external diameter; 6 mm in inner diameter; four C rings and three VF rings; height ratio C:VF = 2:1. The mechanical behavior of the 3D-bioprinted biomimetic trachea under longitudinal tensile and anisotropic compression were analyzed using an FEM program (Ansys software). The alternant structural trachea was divided into stiff units (C rings) and soft units (VF rings). The Young's modulus and Poisson's ratio used for FEM analyses were obtained from the mechanical tests of the corresponding units. The same stress in longitudinal tensile and anisotropic compression was

adopted to compare the deformation or stress distribution of different tracheal models. To simplify the FEM analyses, a linear elastic model was adopted for evaluating the structural and functional differences in this study.

2.8. Cell viability

Rabbit auricles were obtained from autologous rabbits under aseptic conditions. Chondrocytes were isolated from the rabbit auricular cartilage tissue, while fibroblasts were isolated from auricular skin dermis. Cells were expanded to the second passage according to a previous protocol [38]. Chondrocytes and fibroblasts were respectively mixed with the corresponding gel precursors at a density of 1.0×10^7 cells mL^{-1} at 37°C . After 1, 4, and 7 days of culture, the cell viability of cell-laden hydrogel constructs was evaluated using the Live & Dead Cell Viability Assay (Dojindo) following the manufacturer's instructions and examined using a CLSM (Leica TCS SP8 STED 3X). Additionally, cytocompatibility was examined using CCK-8 assay (Dojindo) according to the manufacturer's protocol, and the optical density (OD) was measured with microplate reader (Synergy H1, BioTek) at wavelength of 450 nm.

2.9. Biological functional evaluation

Chondrocytes were cultured in medium containing GM, CM and blank for 7 days, while fibroblasts and endothelial cells were cultured in medium containing GM, EM and blank for 7 days. The corresponding chondrogenic, fibrogenic, and angiogenic functional evaluations were examined *via* immunofluorescent staining as previously described [39]. Col II expression of chondrocytes, α -SMA expression of fibroblasts, and CD31 expression of HUVECs were respectively examined using a CLSM (Leica TCS SP8 STED 3X). After *in vitro* culturing the cell-laden hydrogel constructs for 7 days, total RNA of cells was isolated using TRIzol reagent (Life Technologies) following the manufacturer's protocol. RNA concentration was measured using a Nanodrop (Thermo Scientific). Reversetranscription was performed with a cDNA synthesis kit (Thermo Scientific) following manufacturer's instructions. Gene expressions were analyzed quantitatively with SYBR-green using 7500 Real-Time PCR system (Applied Biosystems, Life Technologies). The primers and probes for *Col II*, *ACAN*, *SOX9*, α -*SMA*, *FAP*, *Vimentin*, *CD31*, *VEGF*, and *GAPDH* were used based on published gene sequences (NCBI and PubMed). The mRNA expression level for each gene was normalized with *GAPDH*. Additionally, the immunofluorescent staining of *SOX9* for chondrocytes in **GC-gel** and α -*SMA* for fibroblasts in **GE-gel** were respectively observed by a CLSM (Leica TCS SP8 STED 3X).

2.10. 3D-bioprinting of CVFIT

For 3D-bioprinting of CVFIT, two bioinks were loaded separately into 5 mL syringes equipped with 0.21 mm diameter needles. The syringes were then mounted into the syringe pump extruder on a 3D BioArchitect work station (Regenovo). Temperatures of syringes and the platform were maintained at $16 \pm 1^\circ\text{C}$. Light irradiation (365-nm LED , 20 mW cm^{-2}) was applied during the switching of extruders. Printing parameters were used as follows: line gap: $500\ \mu\text{m}$; layer thickness: $200\ \mu\text{m}$; photocrosslinking time: 30 s per ring ; pneumatic pressure: 0.18 MPa for **GC-gel** and 0.12 MPa for **GE-gel**; extrusion speed: 6 mm s^{-1} for both **GC-gel** and **GE-gel**.

For cell-free printing, gel precursors were directly printed and dyed with rhodamine (red) for **GC-gel** and Aniline blue (blue) for **GE-gel** respectively. For cell-laden bioprinting, two type of cells (chondrocytes and fibroblasts) were firstly mixed homogeneously into the corresponding gel precursors. The C rings were bioprinted using **GC-gel** with $1 \times 10^8\text{ mL}^{-1}$ of chondrocytes and VF rings were bioprinted using **GE-gel** with $5 \times 10^7\text{ mL}^{-1}$ of fibroblasts respectively. The bioprinted constructs were incubated in Dulbecco's modified eagle medium (DMEM), supplemented with 10% fetal bovine serum (FBS) and 1% penicillin/

streptomycin in a 37°C and 5% CO_2 immediately after bioprinting. Each step was strictly performed under sterile conditions. The whole trachea fluorescence images were acquired by lightsheet fluorescence microscopy (LSFM) (Lightsheet Z.1, Zeiss). 3D reconstruction images and videos were performed with Arivis Vision 4D and Imaris according to the previous methods [14]. The relative fluorescent intensity of C-shape CVFIT was analyzed by the ImageJ software (National Institutes of Health).

2.11. In vivo subcutaneous implantation of nude mice

Female nude mice (6-week-old) were divided into two groups for subcutaneous implantation of 3D-bioprinted biomimetic trachea: C-shape CVFIT as the experimental group ($n = 4$); O-shape CVFIT as the control group ($n = 4$). For both groups, silicon tubes (6 mm external diameter) with similar length of 3D-bioprinted biomimetic trachea were inserted as the internal mechanical support. After certain time points (8 and 16 weeks) of *in vivo* subcutaneous implantation, the regenerated tracheal samples were collected for the following qualitative and quantitative evaluations. C rings: **GC-gel** (5% w/v GelMA/1% w/v CSMA) loaded with $1 \times 10^8\text{ mL}^{-1}$ of chondrocytes; VF rings: **GE-gel** (5% w/v GelMA/1% w/v ElaMA) loaded with $5 \times 10^7\text{ mL}^{-1}$ of fibroblasts.

2.12. Instant segmental trachea reconstruction of rabbits

New Zealand white rabbits (3-month-old) were used to evaluate the feasibility of instant segmental trachea reconstruction using 3D-bioprinted biomimetic CVFIT ($n = 4$). Briefly, the biomimetic CVFIT was firstly 3D-bioprinted by autologous chondrocytes and fibroblasts-loaded tissue-specific matrix hydrogels, and then stacked on a silicon tube for the following use. The segmental trachea defects of rabbits were created as 10 mm length and directly repaired by *in situ* end-to-end anastomosis surgery, in which the ends of the native trachea sew with 5-0 absorbable sutures. After 8 weeks post-operation, total rabbits were euthanized for further evaluation.

2.13. Histological and immunofluorescence staining

All the samples were fixed in 4% paraformaldehyde, embedded in paraffin, and then sectioned. The reconstructed trachea of both transverse and longitudinal regions was respectively stained with hematoxylin and eosin (H&E), Safranin-O (SO), and Masson's trichrome (MT) to evaluate the regenerated tissue structure. The immunofluorescence staining of COL II (green), α -SMA (red), CD31 (orange), and cell nuclei (DAPI, blue) were further used to show the cartilage and fibrous tissue-specific ECM deposition. The keratin (green, K) staining was used to reveal the regeneration of tracheal epithelium.

2.14. Biochemical and mechanical evaluations

The samples (regenerated and native trachea segments) were minced to evaluate cartilage-related biochemical components. Briefly, the contents of total collagen and GAG were respectively quantified by hydroxyproline and Alcian blue colorimetric assay according to the manufacturer's protocols. The compressive properties were measured using a mechanical analyzer (Instron-5542). Briefly, each sample was subjected to a compression cycle with a continuous planar unconfined strain rate of 1 mm min^{-1} up to a maximum of 60% of the deformation, and the compressive modulus was calculated according to the linear region of the stress-strain curve.

2.15. Statistical analyses

Data ($n = 4$) were expressed as the means \pm standard deviations. A one-way analysis of the variance was used to determine the statistical significance of the difference between groups using GraphPad Prism

7.00 software, and a p -value <0.05 was considered statistically significant.

3. Results

3.1. Characterization of photocrosslinkable matrix hydrogels

In this study, photocrosslinkable natural polymers of GelMA (GM), CSMA (CM), and ElaMA (EM) were chosen as hydrogel components owing to the advantages such as ECM-mimicking constitution, biosafety, and ease of preparation. The successful grafting of methacryloyl groups of these polymers were confirmed by ^1H nuclear magnetic resonance (NMR) (Fig. S1). To mimic the tissue-specific constitution, proteoglycan-containing GM polymer and cartilage-derived CM polymer were combined to prepare the cartilage-specific matrix gel (GC-gel), while GM polymer and connective tissue-derived EM polymer were combined to prepare the fibrous tissue-specific matrix gel (GE-gel), and GelMA hydrogel (G-gel) was used as the control. As shown in Fig. 1A, both GC-gel and GE-gel precursors were rapidly crosslinked upon light irradiation (365-nm LED, 20 mW/cm^2), which is suitable for light-assisted extrusion-based 3D-bioprinting. The ^1H NMR spectra demonstrated

that the signals of gel precursors at approximately 5.0–6.0 ppm decreased after light irradiation, indicating successful photopolymerization of multicomponent polymers (Fig. 1B). Time sweep rheological measurements further confirmed the rapid sol-to-gel transition of both GC-gel and GE-gel precursors (Fig. 1C). Noticeably, the gel point of GC-gel (3.4 ± 0.2 s) was shorter than that of G-gel (5.4 ± 0.2 s), while the shear modulus of GC-gel (3.9 ± 0.3 KPa) was greater than that of G-gel (0.9 ± 0.1 KPa) because the crosslinked density of the CM network was higher than that of the GM network (Fig. 1D and E). However, the gel point of GE-gel (9.1 ± 0.4 s) was relatively longer than that of G-gel and the shear modulus of GE-gel (0.7 ± 0.05 KPa) was slightly lower than that of G-gel because the crosslinked density of the EM network was lower than that of the GM network. As shown in Fig. 1F, G and S2, both GC-gel and GE-gel with reasonable swelling ratios (GC-gel: $131 \pm 3\%$; GE-gel: $161 \pm 3\%$) hardly degraded in the PBS solution, but quickly degraded in the collagenase solution due to the enzyme-mediated degradation characteristics, demonstrating satisfactory physicochemical properties as tissue-engineered scaffolds. Moreover, the lyophilized matrix hydrogels were porous after freeze drying, which was consistent with the crosslinked density of the corresponding gel network (Fig. 1H). Additionally, interfacial integration between C-C

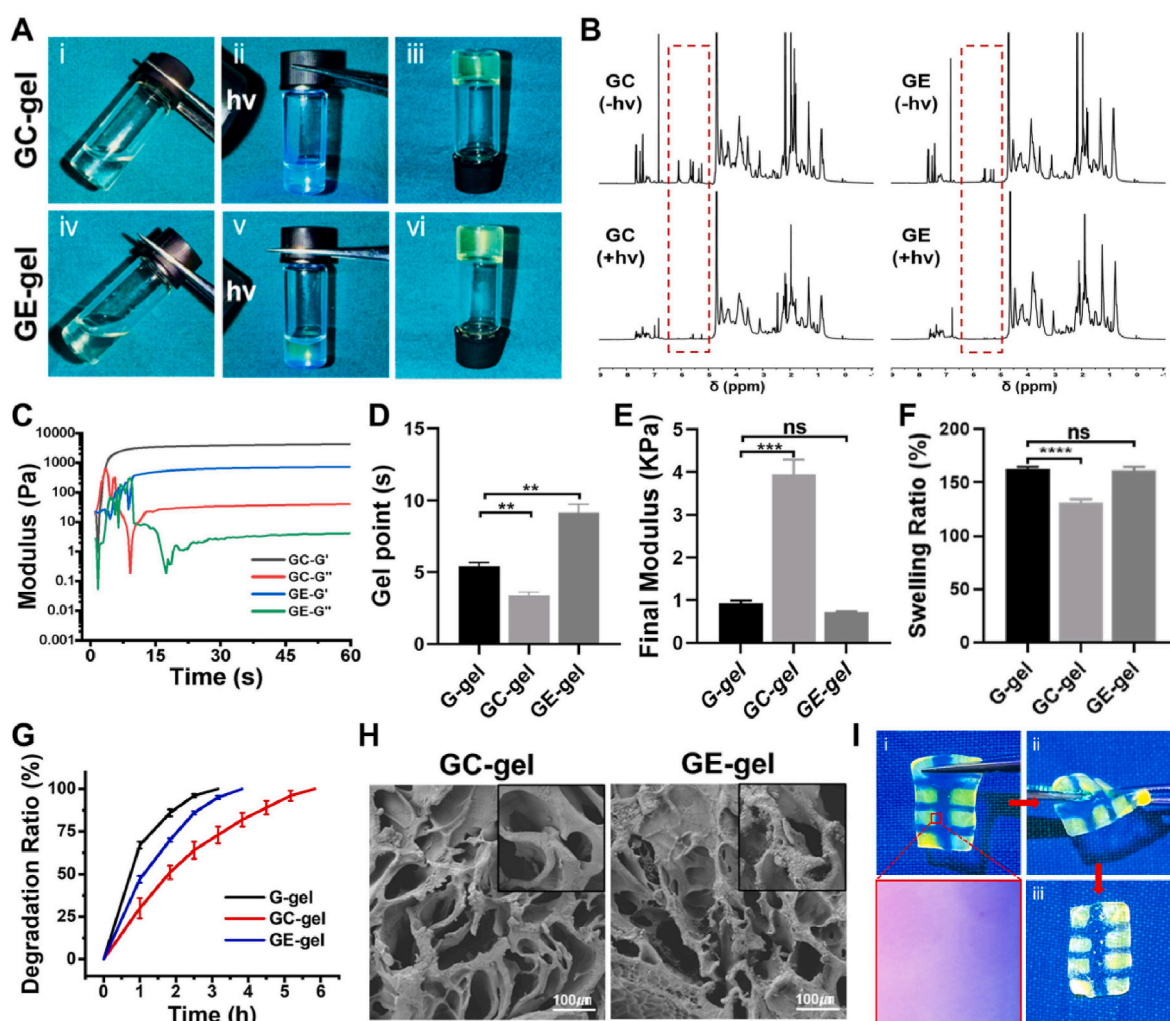


Fig. 1. Characterization of photocrosslinkable matrix hydrogels. A) Photographs showing the sol-to-gel transition upon light irradiation. B) ^1H NMR spectra of GC-gel and GE-gel formulations following photopolymerization with light irradiation. C) Representative rheological analyses of GC-gel and GE-gel formulations. D, E) Statistical analyses of the gel points (D) and final storage moduli (E) of G-gel, GC-gel, and GE-gel. F, G) Swelling ratio in the PBS solution (F) and enzyme-mediated degradation rate in the collagenase solution (G) of G-gel, GC-gel, and GE-gel. H) Scanning electron microscopy images of GC-gel and GE-gel. I) Photographs of the interfacial integration of dye-stained GC-gel (red) and GE-gel (blue) for visualization. The original state was recovered even after stretching and twisting. G-gel: 5% w/v GM; GC-gel: 5% w/v GM/1% w/v CM; GE-gel: 5% w/v GM/1% w/v EM; light irradiation: 365-nm LED, 20 mW/cm^2 .

and VF rings was analyzed qualitatively. As shown in Fig. 1I, the constructs of comprising alternating GC-gel and GE-gel showed structural integrity even after stretching and twisting, which was ascribed to sequential photopolymerization at the interface as well as the firm interconnection of GE-gel and GC-gel.

3.2. Analyses of anisotropic structural design

To highly mimic the alternating stiff-to-soft tissue architecture of the trachea, we meticulously designed two types of matrix hydrogels with different mechanical strength. As shown in Fig. 2A–C, both GC-gel and GE-gel withstood compression of up to approximately 95% owing to the ductile network of GM with a low grafting ratio (~45%), which enabled adaption to physiologically dynamic movements of the native trachea.

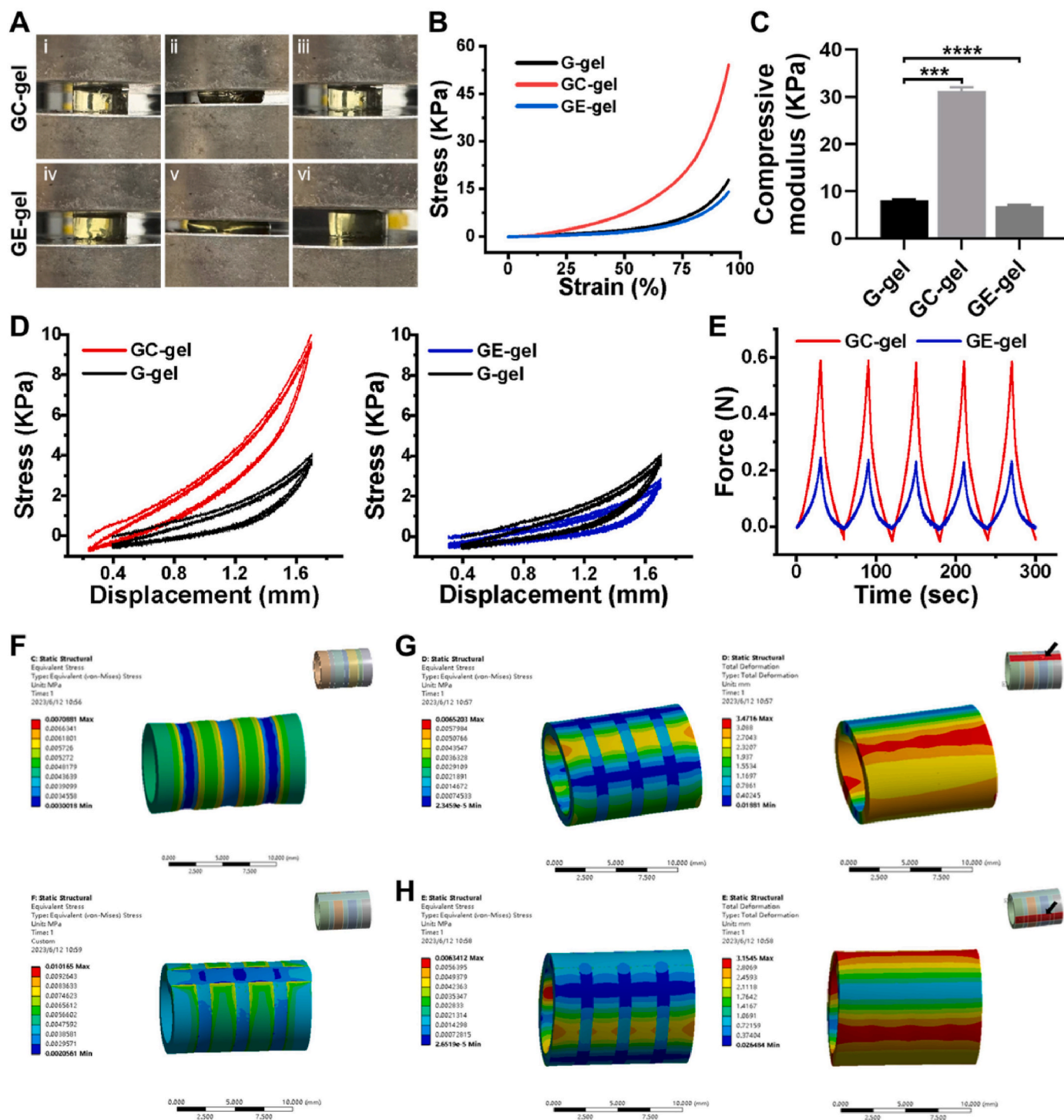


Fig. 2. Analyses of anisotropic structural design. A) Photographs of GC-gel and GE-gel under compression, showing no breakage even under ~90% strain. B, C) Representative compressive stress-strain curves (B) and compressive moduli (C) of G-gel, GC-gel, and GE-gel. D) Representative cyclic compression curves of both GC-gel and GE-gel compared to G-gel. E) Representative repeated compression tests of GC-gel and GE-gel (5 times at 60% strain). F–H) Finite element analyses of C-shape and S-shape structure with longitudinal tensile and anisotropic compression. The hydrogel compositions are the same as shown in Fig. 1.

However, introducing the high-crosslinked **CM** network into the soft **GM** network significantly enhanced the compressive modulus from 8.0 ± 0.1 KPa to 31.2 ± 0.8 KPa, whereas introducing the low-crosslinked **EM** network slightly decreased the compressive modulus to 6.8 ± 0.3 KPa. The same results were observed for repeated compressive cycle tests that the mechanical strength of **GC-gel** was higher than that of **GE-gel** even after three compressive cycles (Fig. 2D). Additionally, there was no obvious decline in the mechanical strength at ~60% strain after five compressive cycles for both **GC-gel** and **GE-gel** (Fig. 2E). Another important consideration is whether the C-shape structural design has unique advantages for trachea reconstruction. Therefore, both C-shape and O-shape tracheal models were evaluated by finite element analysis. As shown in Fig. 2F, the interconnecting C-shape structural design effectively enhanced the integration between **VF** and C-C rings, even under external force loading. Most importantly, the C-shape tubular structure not only bears mechanical compression loaded parallel to the C-shape position dependent on stiff C-C rings, but it also dissipates compressive force loaded perpendicular to the C-shape position owing to the soft gap between the stiff regions (Fig. 2G and H). The above results demonstrated that the alternating stiff-to-soft tubular structure was readily realized using **GC-gel** as the stiff portion and **GE-gel** as the soft portion, and thus facilitated the construction of biomimetic trachea adaptable to anisotropic mechanical environment.

3.3. Biological evaluation of tissue-specific matrix hydrogels

To prepare tissue-specific bioinks for 3D-bioprinting biomimetic trachea, chondrocytes were encapsulated in **GC-gel** as cartilage-specific bioinks, while fibroblasts were encapsulated in **GE-gel** as fibrous tissue-specific bioinks. First, the cytocompatibility of tissue-specific bioinks was evaluated using cell counting kit-8 (CCK-8) and live/dead staining. As shown in Fig. 3A and B, these photocrosslinkable natural polymers (**GM**, **CM**, and **EM**) and corresponding hydrogels (**GC-gel** and **GE-gel**) did not show cytotoxicity, indicating favorable cytocompatibility of photocrosslinkable matrix hydrogels. Additionally, both chondrocytes and fibroblasts displayed a tendency for cell proliferation whether they were cultured in two-dimensional Petri dish or the corresponding three-dimensional hydrogels. Notably, fibroblasts in **GE-gel** exhibited more spreading than chondrocytes in **GC-gel** after 7 days of culturing. This is mainly related to the mechanical microenvironment in different hydrogels that the high-crosslinked **GC** network restricts chondrocyte behavior, whereas the low-crosslinked **GE** network facilitates fibroblast spreading, which is consistent with the native growth ways of these cell types. As shown in Fig. 3C and Fig. S3, fluorescent staining revealed that cartilage-specific expression of type II collagen (COL II) in **CM** groups was stronger than that in **GM** groups. Moreover, fibrous tissue-specific expression of α -smooth muscle actin (α -SMA) and blood vessel-specific expression of platelet endothelial cell adhesion molecule-1 (CD31) in **EM** groups were stronger than those in **GM** groups. These results were further confirmed by real-time quantitative polymerase chain reaction (q-PCR). Specifically, chondrogenic gene expressions (*COL II*, *ACAN*, and *SOX9*) in **CM** groups as well as fibrogenic gene expressions (α -SMA, *FAP*, and *vimentin*) and angiogenic gene expressions (*CD31*) in **EM** groups were significantly up-regulated compared with those in the corresponding control groups (Fig. 3D–F). Thus, with the establishment of tissue-specific biological microenvironment, the chondroitin sulfate-containing **CM** component provides cartilage-specific regulatory function, while the elastin-containing **EM** component offers fibrous tissue-specific regulatory function. Similarly, fluorescent staining of cell-loaded hydrogels also showed tissue-specific protein expressions by chondrocytes (SOX9, green) in **GC-gel** and fibroblasts (α -SMA, red) in **GE-gel**, further indicating satisfactory phenotype-maintainable microenvironment in three-dimensional hydrogels (Fig. 3G). All these results demonstrate that our photocrosslinkable matrix hydrogels are conducive to cell survival, proliferation, and spreading, as well as definitive tissue-specific regulatory functions according to the different

mechanical and biological microenvironment.

3.4. Characterization of 3D-bioprinted biomimetic CVFIT

The printability of tissue-specific bioinks is an essential requirement for 3D-bioprinting biomimetic CVFIT. As shown in Fig. 4A, both **GC-gel** and **GE-gel** showed temperature-dependent gel-transition points at approximately 16 °C, which indicated inherent printability for extrusion-based 3D-bioprinting to sustain the predesigned shape. The printing parameters (applied pressure and printing speed) were optimized by printing test lines. As shown in Fig. 4B, the applied pressure and printing speed were respectively optimized to 0.16 MPa and 8 mm/s for **GC-gel** and 0.14 MPa and 6 mm/s for **GE-gel**. Thus, both O-shape and C-shape CVFIT constructs were printed using a dual-nozzle extrusion-based 3D bioprinting system, and followed by light irradiation (365-nm LED, 20 mW/cm²) to further enhance the mechanical stability of the predesigned shape (Fig. 4C and D). Noticeably, the printing time was shortened to approximately 8 min for O-shape CVFIT constructs and approximately 19 min for C-shape CVFIT constructs by simplifying the printing paths, and thus facilitated instant trachea defect repair surgery. The printed O-shape biomimetic trachea exhibited an alternating structure of C rings-to-VF rings tubular structure, while the printed C-shape CVFIT construct displayed the C-shape structure of alternating C rings and wholly interconnected VF rings across the C rings (C rings: red; VF rings: blue). Furthermore, fluorescently labeled chondrocytes (red) and fibroblasts (green) were precisely localized in the ring-to-ring structure, confirming the control of cell localization and manufacture of 3D morphology according to the predesigned tracheal model (Fig. 4E–G and Video S1). Additionally, the printing procedure had no significant effect on cell viability (**GC-gel**: $95 \pm 1\%$; **GE-gel**: $95 \pm 1\%$) and the mechanical strength of hydrogels (**GC-gel**: 30 ± 1 KPa; **GE-gel**: 6 ± 1 KPa), which was conducive to cell-laden 3D bioprinting (Fig. 4H and I).

3.5. In vivo subcutaneous implantation of 3D-bioprinted CVFIT in nude mice

To investigate the feasibility of *in vivo* trachea regeneration, 3D-bioprinted CVFIT internally supported by a silicone tube (C-shape CVFIT as experimental group; O-shape CVFIT as control group) was subcutaneously implanted in nude mice. After 8 and 16 weeks, the tubular structure of the regenerated trachea was well maintained, which depended on the initial mechanical strength of the construct together with the inner silicone tube support. Additionally, the alternating architecture of regenerated cartilage and fibrous tissue as well as the C-shape cartilage gap of the regenerated trachea were clearly observed (Fig. 5A). As shown in Fig. 5B–E, both regenerated C-shape and O-shape trachea exhibited similar mechanical properties, namely radial compressibility, lateral flexibility, and fatigue resistance, which depended on the mature cartilage and fibrous tissue regenerated during the 8 weeks of subcutaneous implantation (Video S2–3). Notably, the regenerated C-shape trachea possessed unique anisotropic compressibility because the C-shape structural design effectively dissipated mechanical energy, which was conducive to the reconstruction of normal mechanical functions (Video S4). Quantitative analyses further confirmed that the reconstructed mechanical properties as well as the biochemical ECM contents of collagen and glycosaminoglycan were basically similar to those of the native trachea (Fig. 5F–H).

Histological examination of transverse sections showed that the regenerated C-shape trachea contained a C-shape cartilage gap filled with fibrous connective tissue, similar to the native trachea, while the regenerated O-shape trachea contained a single cartilage ring only (Fig. 6A and S4). Histological staining of longitudinal sections showed that both regenerated O-shape and C-shape trachea exhibited an alternating structure of mature cartilage and fibrous tissue (Fig. 6B and S5). Importantly, regeneration of the tissue-specific trachea occurred with

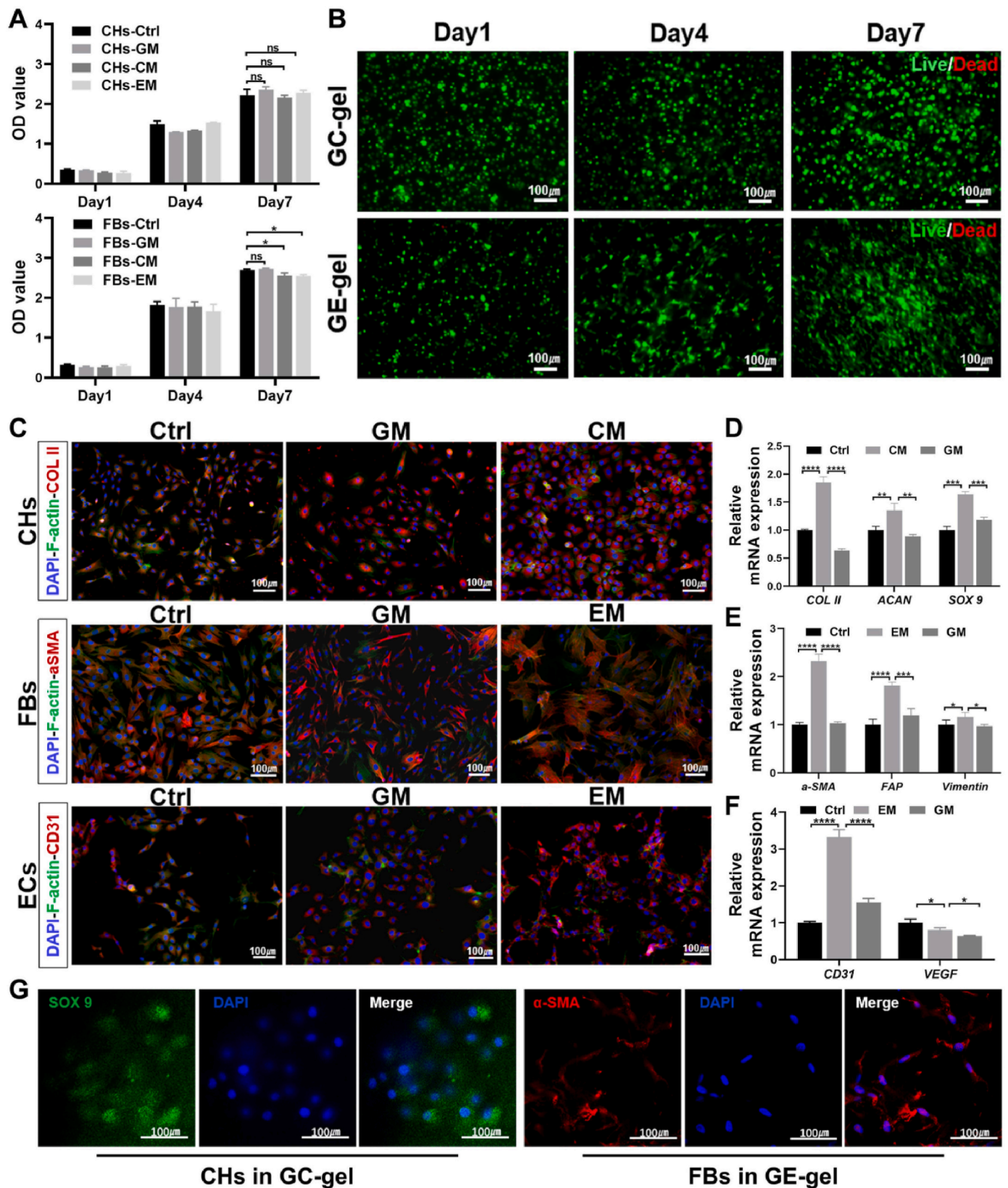


Fig. 3. Biological evaluation of tissue-specific matrix hydrogels. A, B) CCK-8 assays (A) and live/dead staining (B) of chondrocyte-loaded GC-gel and fibroblast-loaded GE-gel bioinks cultured for 1, 4, and 7 days *in vitro*. C) Immunofluorescent staining of COL II (red), F-actin (green), and cell nuclei (DAPI, blue) for chondrogenic marker expressions in CM, GM, and Ctrl groups; α-SMA (red), F-actin (green), and cell nuclei (DAPI, blue) for fibrogenic marker expressions in EM, GM, and Ctrl groups; CD31 (red), F-actin (green), and cell nuclei (DAPI, blue) for vascularized marker expressions in EM, GM, and Ctrl groups. D-F) Relative chondrogenic gene expressions (*COL II*, *ACAN*, *SOX 9*) in cartilage-specific matrix hydrogels as well as fibrogenic gene expressions (*α-SMA*, *FAP*, *Vimentin*) and angiogenic gene expressions (*CD31*, *VEGF*) in fibrous tissue-specific matrix hydrogels. G) Immunofluorescent staining of SOX9 for chondrocytes in GC-gel and α-SMA for fibroblasts in GE-gel respectively. The hydrogel compositions are the same as shown in Fig. 1.

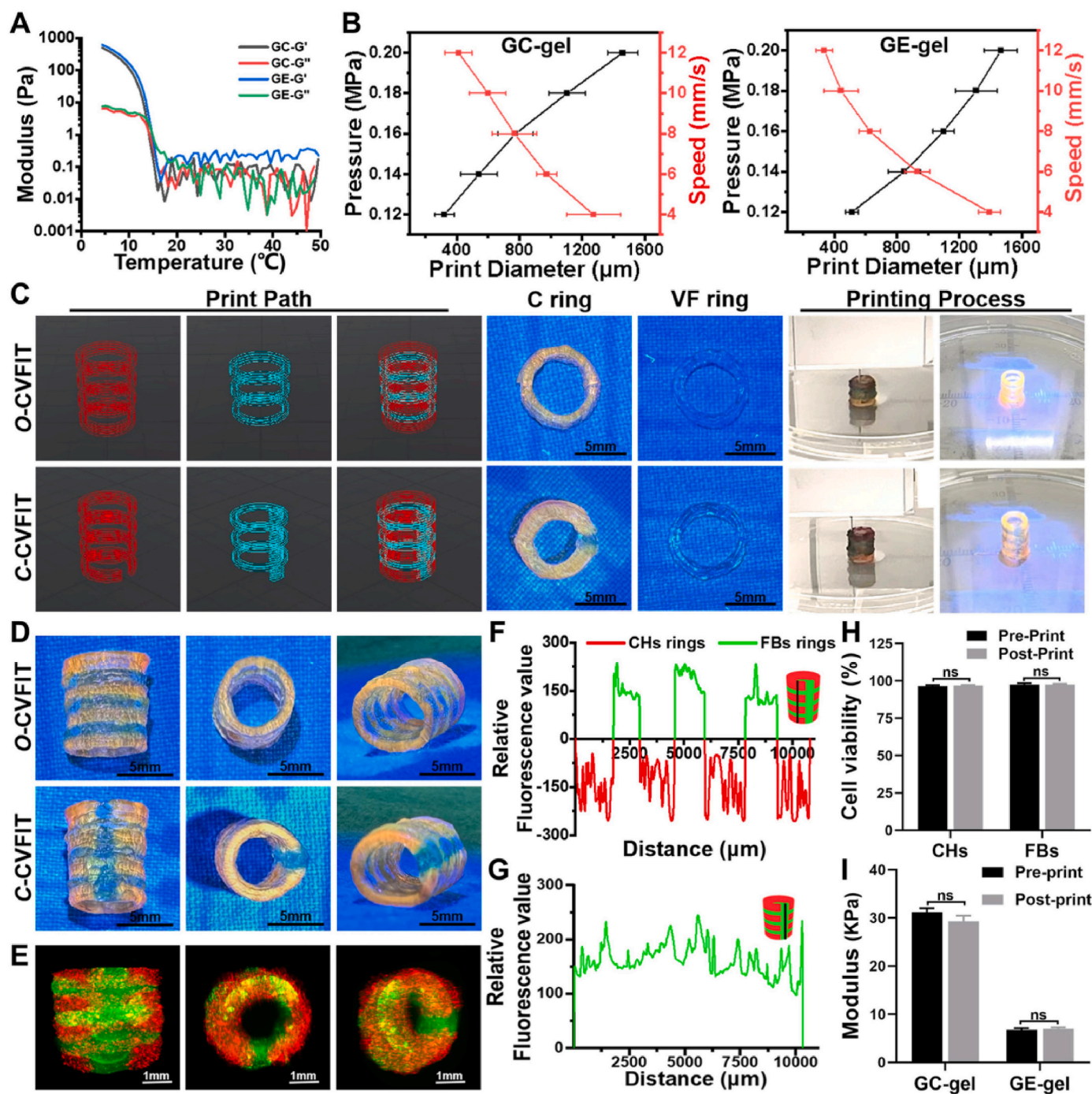


Fig. 4. Characterization of 3D-bioprinted biomimetic CVFIT. A) Temperature-sweep rheological analyses show the printability of GC-gel and GE-gel based on their temperature-sensitive properties. B) Optimization of printing parameters (applied pressure and printing speed) for GC-gel and GE-gel. C) Photographs of 3D-printed paths, C rings, VF rings, and 3D-printing of O-CVFIT and C-CVFIT constructs. D) Photographs of 3D-printed O-CVFIT and C-CVFIT constructs with dyes for visualization (C rings: red; VF rings: blue). E) Representative lightsheet microscopy images of cells distributed in 3D-bioprinted C-CVFIT construct (chondrocytes: green; fibroblasts: red). F, G) Relative fluorescence intensity analyses of different regions of 3D-bioprinted C-CVFIT constructs using ImageJ software. Black lines represent the position of the analytical regions. H) Viability of cells loaded in bioinks with or without extrusion force during 3D-bioprinting. I) Mechanical properties of cell-loaded bioinks before and after 3D-printing. O-CVFIT: O-shape CVFIT; C-CVFIT: C-shape CVFIT.

gradual maturation, and concomitant degradation of the hydrogel scaffolds from 4 weeks to 16 weeks (Fig. S6). At 16 weeks post-implantation, the cartilage region contained typical lacunae and cartilage-specific ECM deposition (safranin-O and COL II staining), while the fibrous region exhibited positive features of Masson's trichrome and α -SMA staining with abundant vascular ingrowth (CD31 staining). Notably, we found that the cartilage tissue adjacent to the fibrous region was more mature than that inside the cartilage region,

indicating that the vascularized fibrous tissue provided sufficient nutrition transport for tracheal cartilage regeneration (Fig. S7). These results demonstrated that the regenerated C-shape trachea successfully enabled reconstruction of both mechanical and physiological functions similar to the native trachea (Fig. S8).

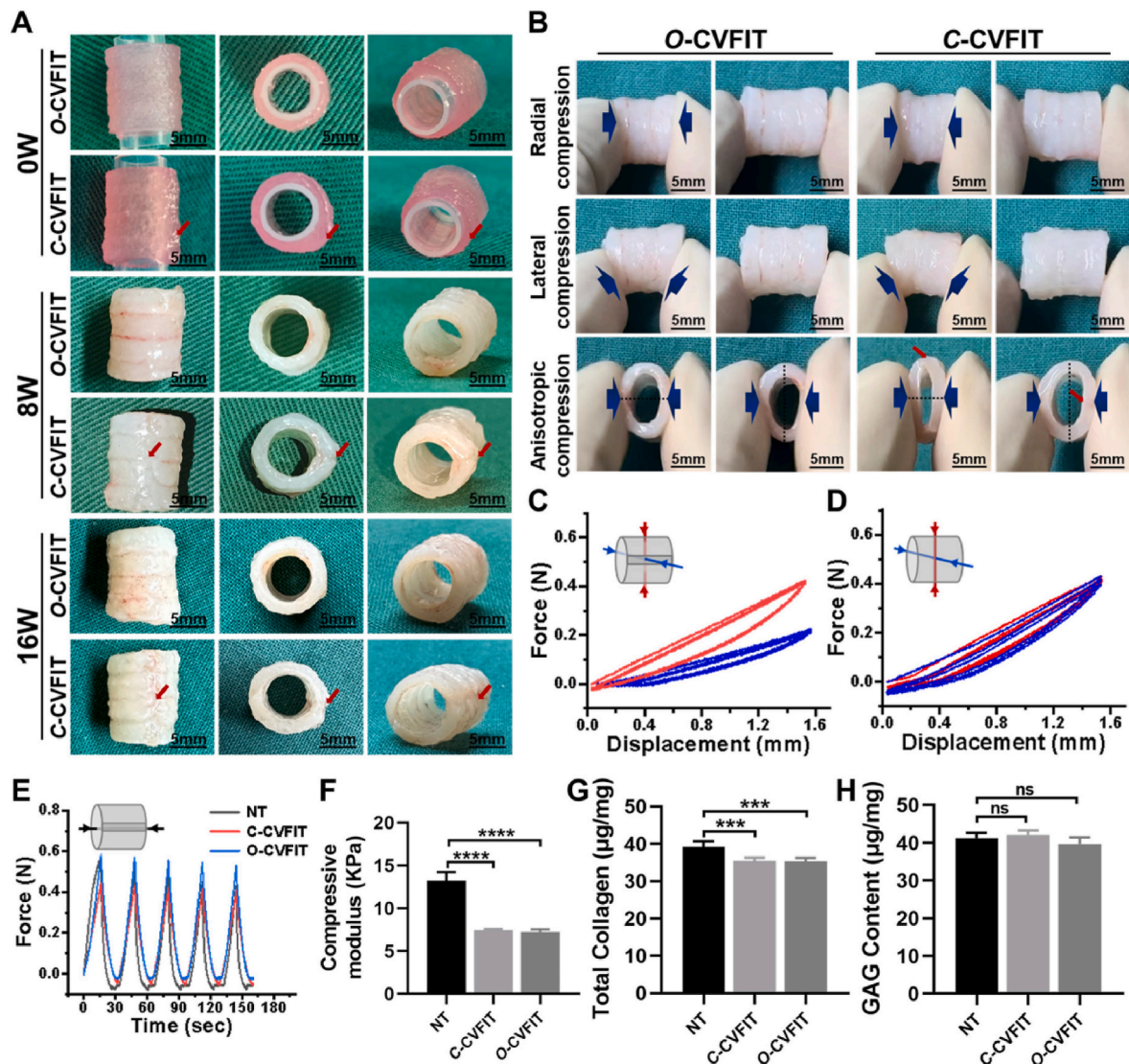


Fig. 5. *In vivo* subcutaneous implantation of 3D-bioprinted CVFIT in nude mice. A) Gross view of 3D-bioprinted O-CVFIT and C-CVFIT constructs as well as the regenerated trachea at 8- and 16-weeks subcutaneous post-implantation. B) Mechanical properties of the regenerated trachea under radial, lateral, and anisotropic compression. Blue arrows represent the direction of compression forces; red arrows represent the position of C-shape cartilage rings. C, D) Representative cyclic compression curves of the regenerated C-shape trachea (C) at both vertical and parallel directions to C-shape cartilage rings, with the O-shape trachea (D) as the control. E) Representative repeated compression tests of regenerated O-shape and C-shape trachea as well as the native trachea. F-H) Statistical analyses of compressive moduli (F), total collagen contents (G), and GAG contents (H) of regenerated O-shape and C-shape trachea as well as the native trachea. O-CVFIT: O-shape CVFIT; C-CVFIT: C-shape CVFIT; NT: native trachea.

3.6. Instant segmental trachea repair by direct end-to-end anastomosis

The feasibility of *in situ* segmental trachea repair was further evaluated by instant trachea reconstruction using 3D-bioprinted C-shape CVFIT in a rabbit model (Fig. 7A). As shown in Fig. 7B, the 3D-bioprinted biomimetic trachea was applied to directly repair segmental trachea defects through one-step end-to-end anastomosis surgery without *in vivo* intramuscular pre-implantation, and thus facilitate instant trachea reconstruction by 3D-bioprinting technique. At 8-weeks post-operation, the reconstructed trachea showed a complete and continuous tubular structure with a smooth internal surface and ventilation, which was seamlessly integrated with the native trachea. Histological examination revealed that the alternating tissue-specific architecture exhibited C-shape cartilage characteristics and fibrous tissue ingrowth. Moreover, the reconstructed trachea showed typical lacunae structure with cartilage-specific ECM deposition in the cartilage region as well as mature fibrous tissue with abundant blood vessels

infiltration in the fibrous tissue region (Fig. 7C–E). Although the regenerated tracheal cartilage partially overlapped with the native trachea, they were integrated well with each other that connected by the regenerated fibrous tissue (Fig. S9). In addition, keratin positive staining of tracheal epithelial cells was observed in the regenerated tracheal lumen, indicating satisfactory epithelial tissue regeneration owing to the recovery of physiological functions (Fig. 7F). Therefore, the current study demonstrated the feasibility of instant and efficient trachea reconstruction using 3D-bioprinted C-shape biomimetic trachea as an alternative treatment for segmental trachea defect repair.

4. Discussion

Currently, multicellular 3D-bioprinting technique has emerged as an attractive strategy to construct heterogeneous biomimetic trachea with native-like tissue architecture [40–43]. To date, there is still limited breakthrough to realize segmental trachea reconstruction using

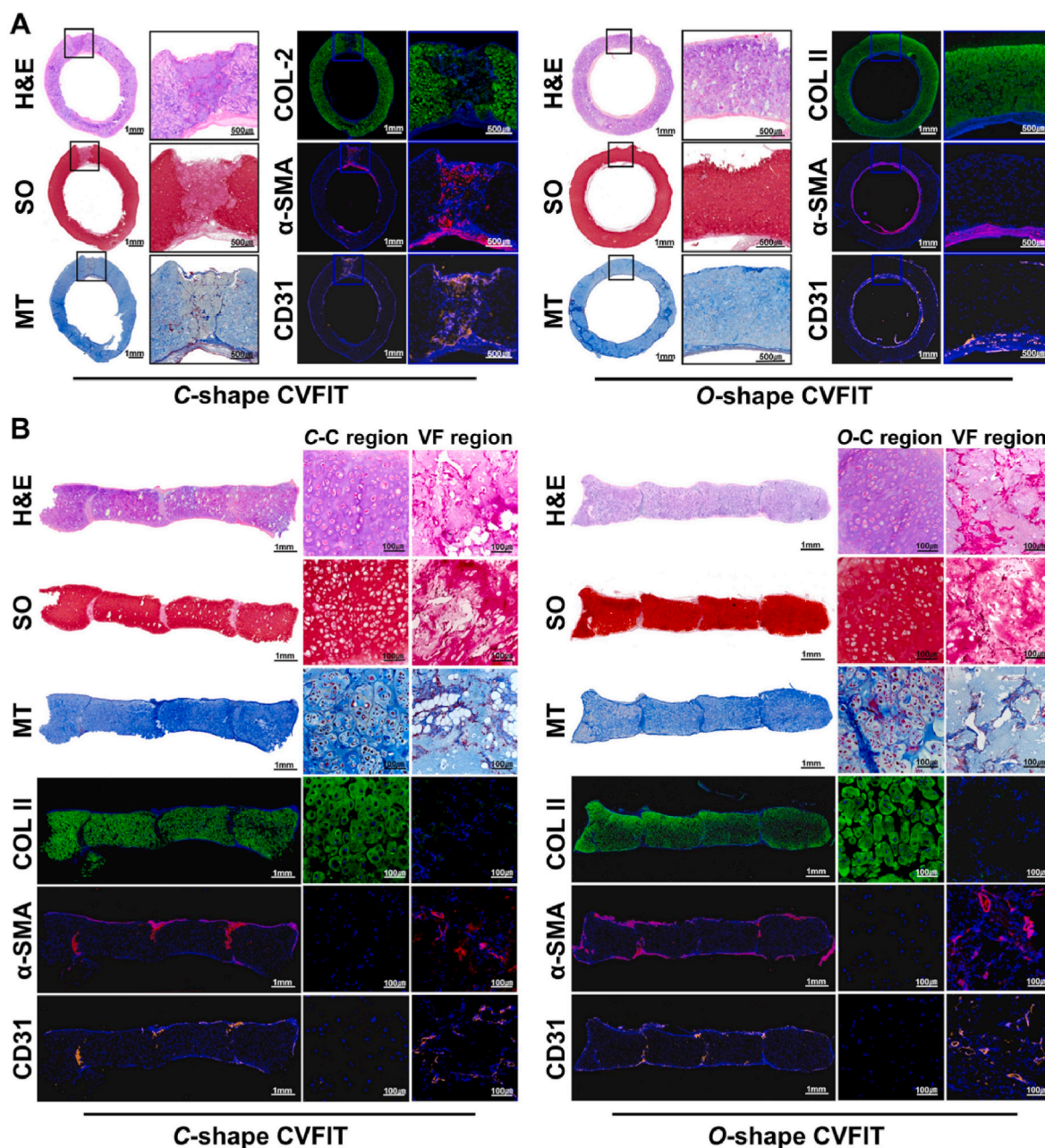


Fig. 6. Histological examinations of the regenerated trachea in nude mice. A, B) Histological staining of H&E, safranin-O (SO), and Masson’s trichrome (MT), as well as immunofluorescence staining of COL II (green), α -SMA (red), CD31 (orange), and cell nuclei (DAPI, blue) of the regenerated trachea in the transverse (A) and longitudinal (B) sections at 16-weeks post-implantation.

3D-bioprinted biomimetic trachea. As far as we know, the key difficulties lie in the lack of ideal bioinks, the requirement for precise structural biomimicking, and the complexity of multi-step surgical procedures [44–46]. To address the above problems, we first adopted hybrid photocrosslinking method to prepare two types of tissue-specific matrix hydrogels with desired mechanical and biological microenvironment. Then, 3D-bioprinted biomimetic CVFIT comprising alternating C-shape C and VF rings was meticulously designed with optimal printing paths and 3D models. Most importantly, we proposed an instant one-step method, namely direct end-to-end anastomosis, for segmental trachea reconstruction to avoid secondary surgery. Eventually, instant and efficient trachea defect repair using 3D-bioprinted biomimetic CVFIT was successfully verified in rabbit models.

The primary consideration for 3D-bioprinting C-shape biomimetic CVFIT is to prepare ideal bioinks with chondrogenic and fibrogenic

microenvironment. As tissue-specific bioinks, the requirements of matrix hydrogels are based on: i) simple constitution for ease of preparation; ii) different mechanical strength to match the alternating stiff-to-soft tissue architecture; and iii) tissue-specific induced microenvironment for both cartilage and fibrous tissue regeneration. In the current hydrogel design, we applied our previously established hybrid photocrosslinking method to construct matrix hydrogels with ECM-mimicking constitution. To simplify the complicated hydrogel composition of our previous design [14], cartilage-derived CM and connective tissue-derived EM polymers were introduced into proteoglycan-containing GM constitution as cartilage-specific and fibrous tissue-specific matrix hydrogels respectively. Noticeably, two types of matrix hydrogels similarly possessed biomimetic tissue-specific mechanical and biological microenvironment, which were suitable for the growth ways of both cartilage and fibrous tissues. The current study

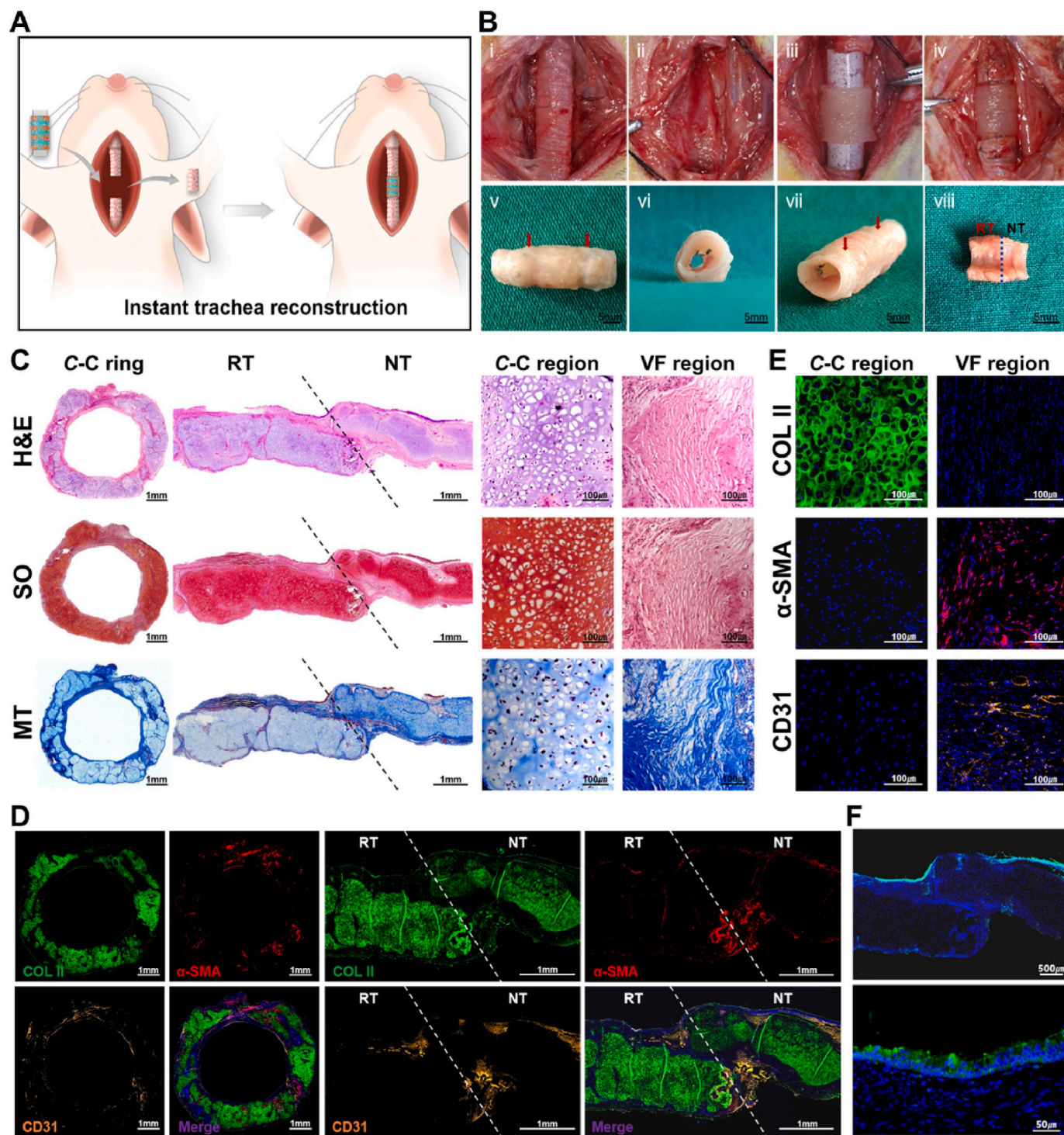


Fig. 7. Instant segmental trachea repair by direct end-to-end anastomosis in rabbits. A) Schematic illustration of segmental trachea defect repair by direct end-to-end anastomosis. B) Photographs of the surgical procedures of direct end-to-end anastomosis to repair segmental trachea defects (i-iv) and gross view of the reconstructed trachea segment at 8-weeks post-surgery (v-viii). Red arrows represent the reconstructed trachea. Blue dotted line represents the regenerated interface between RT and NT. C-E) Histological staining of H&E, Safranin-O (SO), and Masson’s trichrome (MT), as well as immunofluorescence staining of COL II (green), α -SMA (red), CD31 (orange), and cell nuclei (DAPI, blue) in both transverse and longitudinal sections of the reconstructed trachea at 8-weeks post-surgery. F) Immunofluorescence staining of keratin (green) shows regeneration of the tracheal epithelium at 8-weeks post-surgery. RT: reconstructed trachea; NT: native trachea.

showed that the high-crosslinked GC network provided mechanical support, a restricted 3D matrix for chondrocyte survival, and inherent chondrogenic regulation. In contrast, the low-crosslinked GE network provided mechanical ductility, a relaxed 3D matrix for fibroblast spreading, and intrinsic fibrogenic regulation.

Furthermore, the next consideration for 3D-bioprinting C-shape

biomimetic CVFIT is the precise structural design. To precisely mimic the native-like tracheal architecture, we meticulously designed an tubular structure of alternating C-shape C rings and wholly interconnected VF rings. It should be noted that the C-shape design is based on a comprehensive consideration of structural integration, mechanical adaptability, and physiological function. Firstly, the embedding VF rings

into C rings depends on C-shape characteristics to enable the firm structural integration after interfacial photopolymerization of the interpenetrating GC-GE gel network. Additionally, the C-shape tracheal structure effectively dissipates anisotropic forces, which enables adaptation to physiologically dynamic movements, while the O-shape tracheal structure bears isotropic mechanical compression without stress dissipation. Consistent with the finite element analysis, *in vivo* experiments further confirmed reconstruction of favorable mechanical properties, such as lateral bending flexibility and anisotropic compressive resistance. More importantly, histological examination also verified that the C-shape structural design allowed efficient reconstruction of the complete vascular network throughout the whole tubular structure to supply abundant blood and nutrients for bulk cartilage regeneration.

The ultimate purpose of the current study was to achieve segmental trachea defect repair using 3D-bioprinted C-shape biomimetic CVFIT. Recently, some studies have proposed a direct trachea defect repair strategy with cellular or acellular tracheal constructs, which innovatively achieved direct one-step replacement using tissue-engineered trachea [20,47]. In contrast to the conventional two-step method by mean of intramuscular pre-implantation, the one-step surgical mode of direct end-to-end anastomosis has the unique advantages of instant repair and highly efficient tissue regeneration without long-time waiting. In this study, we combined 3D-bioprinted C-shape biomimetic CVFIT with a silicone tube-based inner support to provide sufficient mechanical strength and structural stability for instant repair surgery. Moreover, although intramuscular pre-implantation was omitted, histological evaluation in rabbit models also presented mature cartilage regeneration with an interconnected vascular network. Actually, highly efficient trachea regeneration is attributable to the tissue-specific mechanical and biological microenvironment promoting cartilage and fibrous tissue regeneration. Additionally, precise design of the biomimetic architecture enables mechanical adaptability to physiologically dynamic movements, thus improving the surgical success rate. Although the 3D-bioprinted C-shape biomimetic trachea showed satisfactory results in the current study, there are still some challenges when considering the subsequent translational application. Firstly, the design of pre-epithelialization needs to be considered instead of relying on the migration of its own epithelial cells. In addition, the surgical procedure for instant end-to-end anastomosis should be improved because the overlap between the regenerated trachea and the native trachea is unavoidable at present (Fig. S9). Moreover, it is necessary to further verify the feasibility over a longer period in large animal models for the future clinical application.

5. Conclusion

In summary, we developed a novel strategy for segmental trachea reconstruction through direct end-to-end anastomosis using 3D-bioprinted C-shape biomimetic trachea. In the current study, we easily prepared two types of tissue-specific matrix hydrogels with desired mechanical and biological microenvironment for cartilage and fibrous tissue regeneration. The C-shape tracheal structure of alternating C and VF rings was rapidly 3D-bioprinted by optimizing the printing paths, and thus satisfactorily meet the requirements of structural integration, mechanical adaptability, and physiological function. Furthermore, both *in vivo* trachea regeneration by subcutaneous implantation and *in situ* segmental trachea reconstruction by direct end-to-end anastomosis were successfully achieved using 3D-bioprinted C-shape biomimetic trachea. Although the current work represents a proof-of-concept study, we are fully verified the feasibility of instant and efficient trachea reconstruction strategy by 3D-bioprinting technique, and thus would offer a promising alternative treatment for segmental trachea defects.

Ethics approval and consent to participate

All protocols for experimental in animals were approved by the

Animal Care and Experimental Committee of Shanghai Jiao Tong University School of Medicine (SH9H-2021-A655-SB).

CRedit authorship contribution statement

Yuyan Sun: Methodology, Data curation, Formal analysis, Writing – original draft. **Yingying Huo:** Data curation, Formal analysis, Funding acquisition, Investigation. **Xinyue Ran:** Data curation, Formal analysis, Investigation. **Hongying Chen:** Data curation, Investigation. **Qingqiang Pan:** Formal analysis, Investigation. **Yujie Chen:** Methodology, Formal analysis. **Ying Zhang:** Funding acquisition, Resources. **Wenjie Ren:** Funding acquisition, Investigation. **Xiaoyun Wang:** Project administration, Funding acquisition, Investigation. **Guangdong Zhou:** Conceptualization, Project administration, Funding acquisition, Resources. **Yujie Hua:** Conceptualization, Methodology, Project administration, Writing – review & editing.

Declaration of competing interest

The authors declare no competing interests.

Acknowledgements

This research was financially supported by the National Key Research and Development Program of China (2022YFA1207500), Biomaterials and Regenerative Medicine Institute Cooperative Research Project of Shanghai Jiaotong University School of Medicine (2022LHA07), the National Natural Science Foundation of China (82302823, 81871502 and 81671837), the Key Research and Development Program of Henan Province (221111310100), Major Science and Technology Projects of Xinxiang City (21ZD006), Shanghai Municipal Science and Technology Major Project (21Y11911700), Science and Technology Innovation Action Plan Venus Project (Sailing Special Project, 23YF1421400), the China Postdoctoral Science Foundation (2023M732294), and Shanghai Municipal Key Clinical Specialty (shslczdzk06601). The authors acknowledge Prof. Linyong Zhu's group (Shanghai Jiao Tong University) for the help with materials' characterization. The authors also acknowledge the 3D-bioprinting technical help of Sisi Shen in Shanghai Key Laboratory of Tissue Engineering.

Appendix A. Supplementary data

Supplementary data to this article can be found online at <https://doi.org/10.1016/j.bioactmat.2023.09.011>.

References

- [1] Z. Shen, T. Xia, J. Zhao, S. Pan, Current status and future trends of reconstructing a vascularized tissue-engineered trachea, *Connect. Tissue Res.* (2023) 1–17, <https://doi.org/10.1080/03008207.2023.2212052>. Advance online publication.
- [2] A. Dhasmana, A. Singh, S. Rawal, Biomedical grafts for tracheal tissue repairing and regeneration "Tracheal tissue engineering: an overview", *J. Tissue Eng. Regen. Med.* 14 (5) (2020) 653–672, <https://doi.org/10.1002/term.3019>.
- [3] M.J. McPhail, J.R. Janus, D.G. Lott, Advances in regenerative medicine for otolaryngology/head and neck surgery, *BMJ* 369 (2020) m718, <https://doi.org/10.1136/bmj.m718>.
- [4] Y. Xu, L. Duan, Y. Li, Y. She, J. Zhu, G. Zhou, G. Jiang, Y. Yang, Nanofibrillar decellularized Wharton's jelly matrix for segmental tracheal repair, *Adv. Funct. Mater.* 30 (2020), 1910067, <https://doi.org/10.1002/adfm.201910067>.
- [5] L.G. Griffith, G. Naughton, Tissue engineering—current challenges and expanding opportunities, *Science* 295 (5557) (2002) 1009–1014, <https://doi.org/10.1126/science.1069210>.
- [6] T. Zeng, P. Yuan, L. Liang, X. Zhang, H. Zhang, W. Wu, Cartilaginous extracellular matrix enriched with human gingival mesenchymal stem cells derived "matrix bound extracellular vesicles" enabled functional reconstruction of tracheal defect, *Adv. Sci.* 9 (2) (2022), e2102735, <https://doi.org/10.1002/advs.202102735>.
- [7] W. Sun, Y. Yang, L. Wang, H. Tang, L. Zhang, Y. She, X. Xiao, X. Hu, Q. Feng, C. Chen, Utilization of an acellular cartilage matrix-based photocrosslinking hydrogel for tracheal cartilage regeneration and circumferential tracheal repair, *Adv. Funct. Mater.* 32 (2022), 2201257, <https://doi.org/10.1002/adfm.202201257>.

- [8] P.W. Furlow, D.J. Mathisen, Surgical anatomy of the trachea, *Ann. Cardiothorac. Surg.* 7 (2) (2018) 255–260, <https://doi.org/10.21037/acs.2018.03.01>.
- [9] A. Lee, A. Hudson, D.J. Shiwariski, J.W. Tashman, T.J. Hinton, S. Yerneni, J. M. Bliley, P.G. Campbell, A.W. Feinberg, 3D bioprinting of collagen to rebuild components of the human heart, *Science* 365 (6452) (2019) 482–487, <https://doi.org/10.1126/science.aav9051>.
- [10] F. Akter, Y. Araf, S.K. Promon, J. Zhai, C. Zheng, 3D bioprinting for regenerating COVID-19-mediated irreversibly damaged lung tissue, *Int. J. Bioprint.* 8 (4) (2022) 616, <https://doi.org/10.18063/ijb.v8i4.616>.
- [11] L. Jia, Y. Hua, J. Zeng, W. Liu, D. Wang, G. Zhou, X. Liu, H. Jiang, Bioprinting and regeneration of auricular cartilage using a bioactive bioink based on microporous photocrosslinkable acellular cartilage matrix, *Bioact. Mater.* 16 (2022) 66–81, <https://doi.org/10.1016/j.bioactmat.2022.02.032>.
- [12] S.H. Kim, H. Hong, O. Ajiteru, M.T. Sultan, Y.J. Lee, J.S. Lee, O.J. Lee, H. Lee, H. S. Park, K.Y. Choi, J.S. Lee, H.W. Ju, I.S. Hong, C.H. Park, 3D bioprinted silk fibroin hydrogels for tissue engineering, *Nat. Protoc.* 16 (12) (2021) 5484–5532, <https://doi.org/10.1038/s41596-021-00622-1>.
- [13] M. Cuvellier, F. Ezan, H. Oliveira, S. Rose, J.C. Fricain, S. Langouët, V. Legagneux, L. Baffet, 3D culture of HepaRG cells in GelMa and its application to bioprinting of a multicellular hepatic model, *Biomaterials* 269 (2021), 120611, <https://doi.org/10.1016/j.biomaterials.2020.120611>.
- [14] Y. Huo, Y. Xu, X. Wu, E. Gao, A. Zhan, Y. Chen, Y. Zhang, Y. Hua, W. Swieszkowski, Y.S. Zhang, G. Zhou, Functional trachea reconstruction using 3D-bioprinted native-like tissue architecture based on designable tissue-specific bioinks, *Adv. Sci.* 9 (2022), 2202181, <https://doi.org/10.1002/advs.202202181>.
- [15] J.H. Park, M. Ahn, S.H. Park, H. Kim, M. Bae, W. Park, S.J. Hollister, S.W. Kim, Q. W. Cho, 3D bioprinting of a trachea-mimetic cellular construct of a clinically relevant size, *Biomaterials* 279 (2021), 121246, <https://doi.org/10.1016/j.biomaterials.2021.121246>.
- [16] Y. Xu, J. Dai, X. Zhu, R. Cao, N. Song, M. Liu, X. Liu, J. Zhu, F. Pan, L. Qin, G. Jiang, H. Wang, Y. Yang, Biomimetic trachea engineering via a modular ring strategy based on bone-marrow stem cells and atelocollagen for use in extensive tracheal reconstruction, *Adv. Mater.* 34 (2022), 2106755, <https://doi.org/10.1002/adma.202106755>.
- [17] M. Yang, J. Chen, Y. Chen, W. Lin, H. Tang, Z. Fan, L. Wang, Y. She, F. Jin, L. Zhang, W. Sun, C. Chen, Scaffold-free tracheal engineering via a modular strategy based on cartilage and epithelium sheets, *Adv. Healthcare Mater.* 12 (6) (2023), e2202022, <https://doi.org/10.1002/adhm.202202022>.
- [18] Y. Yu, C.B. Ahn, K.H. Son, J.W. Lee, Motility improvement of biomimetic trachea scaffold via hybrid 3D-bioprinting Technology, *Polymers* 13 (6) (2021) 971, <https://doi.org/10.3390/polym13060971>.
- [19] E. Gao, Y. Wang, P. Wang, Q. Wang, Y. Wei, D. Song, H. Xu, J. Ding, Y. Xu, H. Xia, R. Chen, L. Duan, C-shaped cartilage development using Wharton's jelly-derived hydrogels to assemble a highly biomimetic neotrachea for use in circumferential tracheal reconstruction, *Adv. Funct. Mater.* 33 (2023), 2212830, <https://doi.org/10.1002/adfm.202212830>.
- [20] F. Sun, Y. Lu, Z. Wang, B. Zhang, Z. Shen, L. Yuan, C. Wu, Q. Wu, W. Yang, G. Zhang, Z. Pan, H. Shi, Directly construct microvascularization of tissue engineering trachea in orthotopic transplantation, *Mater. Sci. Eng., C* 128 (2021), 112201, <https://doi.org/10.1016/j.msec.2021.112201>.
- [21] J.E. Dennis, K.G. Bernardi, T.J. Kean, N.E. Liou, T.K. Meyer, Tissue engineering of a composite trachea construct using autologous rabbit chondrocytes, *J. Tissue Eng. Regen. Med.* 12 (3) (2018) e1383–e1391, <https://doi.org/10.1002/term.2523>.
- [22] D. Li, Z. Yin, Y. Liu, S. Feng, Y. Liu, F. Lu, Y. Xu, P. Min, M. Hou, K. Li, A. He, W. Zhang, W. Liu, Y. Zhang, G. Zhou, Y. Cao, Regeneration of trachea graft with cartilage support, vascularization, and epithelization, *Acta Biomater.* 89 (2019) 206–216, <https://doi.org/10.1016/j.actbio.2019.03.003>.
- [23] X. Luo, Y. Liu, Z. Zhang, R. Tao, Y. Liu, A. He, Z. Yin, D. Li, W. Zhang, W. Liu, Y. Cao, G. Zhou, Long-term functional reconstruction of segmental tracheal defect by pedicled tissue-engineered trachea in rabbits, *Biomaterials* 34 (13) (2013) 3336–3344, <https://doi.org/10.1016/j.biomaterials.2013.01.060>.
- [24] B. Gao, H. Jing, M. Gao, S. Wang, W. Fu, X. Zhang, X. He, J. Zheng, Long-segmental tracheal reconstruction in rabbits with pedicled Tissue-engineered trachea based on a 3D-printed scaffold, *Acta Biomater.* 97 (2019) 177–186, <https://doi.org/10.1016/j.actbio.2019.07.043>.
- [25] H. Ravanbakhsh, V. Karamzadeh, G. Bao, L. Mongeau, D. Juncker, Y.S. Zhang, Emerging Technologies in multi-material bioprinting, *Adv. Mater.* 33 (2021), 2104730, <https://doi.org/10.1002/adma.202104730>.
- [26] B. Derby, Printing and prototyping of tissues and scaffolds, *Science* 338 (6109) (2012) 921–926, <https://doi.org/10.1126/science.1226340>.
- [27] R.L. Truby, J.A. Lewis, Printing soft matter in three dimension, *Nature* 540 (7633) (2016) 371–378, <https://doi.org/10.1038/nature21003>.
- [28] M. Chen, Y. Li, S. Liu, Z. Feng, H. Wang, D. Yang, W. Guo, Z. Yuan, S. Gao, Y. Zhang, K. Zha, B. Huang, F. Wei, X. Sang, Q. Tian, X. Yang, X. Sui, Y. Zhou, Y. Zheng, Q. Guo, Hierarchical macro-microporous WPU-ECM scaffolds combined with microfracture promote in situ articular cartilage regeneration in rabbits, *Bioact. Mater.* 6 (7) (2020) 1932–1944, <https://doi.org/10.1016/j.bioactmat.2020.12.009>.
- [29] H. Kim, B. Kang, X. Cui, S. Lee, K. Lee, D. Cho, W. Hwang, T. Woodfield, K. Lim, J. Jang, Light-activated decellularized extracellular matrix-based bioinks for volumetric tissue analogs at the centimeter scale, *Adv. Funct. Mater.* 31 (2021), 2011252, <https://doi.org/10.1002/adfm.202011252>.
- [30] D. Visscher, H. Lee, P.P.M. van Zuijlen, M.N. Helder, A. Atala, J.J. Yoo, S.J. Lee, A photo-crosslinkable cartilage-derived extracellular matrix bioink for auricular cartilage tissue engineering, *Acta Biomater.* 121 (2021) 193–203, <https://doi.org/10.1016/j.actbio.2020.11.029>.
- [31] F. Yu, A.U.R. Khan, H. Zheng, X. Li, M. El-Newehy, H. El-Hamshary, Y. Morsi, J. Li, J. Wu, X. Mo, A photocrosslinking antibacterial decellularized matrix hydrogel with nanofiber for cutaneous wound healing, *Colloids Surf., B* 217 (2022), 112691, <https://doi.org/10.1016/j.colsurfb.2022.112691>.
- [32] L. Zhou, L. Fan, F. Zhang, Y. Jiang, M. Cai, C. Dai, Y. Luo, L. Tu, Z. Zhou, X. Li, C. Ning, K. Zheng, A. Boccaccini, G. Tan, Hybrid gelatin/oxidized chondroitin sulfate hydrogels incorporating bioactive glass nanoparticles with enhanced mechanical properties, mineralization, and osteogenic differentiation, *Bioact. Mater.* 6 (3) (2020) 890–904, <https://doi.org/10.1016/j.bioactmat.2020.09.012>.
- [33] H. Park, B. Choi, J. Hu, M. Lee, Injectable chitosan hyaluronic acid hydrogels for cartilage tissue engineering, *Acta Biomater.* 9 (1) (2013) 4779–4786, <https://doi.org/10.1016/j.actbio.2012.08.033>.
- [34] Y. Zhang, R.K. Avery, Q. Vallmajo-Martin, A. Assmann, A. Vegh, A. Memic, B. D. Olsen, N. Annabi, A. Khademhosseini, A highly elastic and rapidly crosslinkable elastin-like polypeptide-based hydrogel for biomedical applications, *Adv. Funct. Mater.* 25 (30) (2015) 4814–4826, <https://doi.org/10.1002/adfm.201501489>.
- [35] C. Zhou, C. Wang, K. Xu, Z. Niu, S. Zou, D. Zhang, Z. Qian, J. Liao, J. Xie, Hydrogel platform with tunable stiffness based on magnetic nanoparticles cross-linked GelMA for cartilage regeneration and its intrinsic biomechanism, *Bioact. Mater.* 25 (2022) 615–628, <https://doi.org/10.1016/j.bioactmat.2022.07.013>.
- [36] C.C.L. Schuurmans, M. Mihajlovic, C. Hiemstra, K. Ito, W.E. Hennink, T. Vermonden, Hyaluronic acid and chondroitin sulfate (meth)acrylate-based hydrogels for tissue engineering: synthesis, characteristics and pre-clinical evaluation, *Biomaterials* 268 (2021), 120602, <https://doi.org/10.1016/j.biomaterials.2020.120602>.
- [37] K. Da Silva, P. Kumar, S.F. van Vuuren, V. Pillay, Y.E. Choonara, Three-dimensional printability of an ECM-based gelatin methacryloyl (GelMA) biomaterial for potential neuroregeneration, *ACS Omega* 6 (33) (2021) 21368–21383, <https://doi.org/10.1021/acsomega.1c01903>.
- [38] Y. Hua, H. Xia, L. Jia, J. Zhao, D. Zhao, X. Yan, Y. Zhang, S. Tang, G. Zhou, L. Zhu, Q. Lin, Ultrafast, tough, and adhesive hydrogel based on hybrid photocrosslinking for articular cartilage repair in water-filled arthroscopy, *Sci. Adv.* 7 (35) (2021), eabg0628, <https://doi.org/10.1126/sciadv.abg0628>.
- [39] T. Wang, W. Xu, X. Zhao, B. Bai, Y. Hua, J. Tang, F. Chen, Y. Liu, Y. Wang, G. Zhou, Y. Cao, Repair of osteochondral defects mediated by double-layer scaffolds with natural osteochondral-biomimetic microenvironment and interface, *Mater. Today Bio* 14 (2022), 100234, <https://doi.org/10.1016/j.mtbio.2022.100234>.
- [40] L. Du, C. Qin, H. Zhang, F. Han, J. Xue, Y. Wang, J. Wu, Y. Xiao, Z. Huan, C. Wu, Multicellular bioprinting of biomimetic inks for tendon-to-bone regeneration, *Adv. Sci.* (2023), e2301309, <https://doi.org/10.1002/advs.202301309>. Advance online publication.
- [41] Y. Liu, K. Zheng, Z. Meng, L. Wang, X. Liu, B. Guo, J. He, X. Tang, M. Liu, N. Ma, X. Li, J. Zhao, A cell-free tissue-engineered tracheal substitute with sequential cytokine release maintained airway opening in a rabbit tracheal full circumferential defect model, *Biomaterials* 300 (2023), 122208, <https://doi.org/10.1016/j.biomaterials.2023.122208>.
- [42] D. Xia, D. Jin, Q. Wang, M. Gao, J. Zhang, H. Zhang, J. Bai, B. Feng, M. Chen, Y. Huang, Y. Zhong, N. Witman, W. Wang, Z. Xu, H. Zhang, M. Yin, W. Fu, Tissue-engineered trachea from a 3D-printed scaffold enhances whole-segment tracheal repair in a goat model, *J. Tissue Eng. Regen. Med.* 13 (4) (2019) 694–703, <https://doi.org/10.1002/term.2828>.
- [43] D. Lei, B. Luo, Y. Guo, D. Wang, H. Yang, S. Wang, H. Xuan, A. Shen, Y. Zhang, Z. Liu, C. He, F. Qing, Y. Xu, G. Zhou, Z. You, 4-Axis printing microfibrous tubular scaffold and tracheal cartilage application, *Sci. China Mater.* 62 (2019) 1910–1920, <https://doi.org/10.1007/s40843-019-9498-5>.
- [44] M. Gao, H. Zhang, W. Dong, J. Bai, B. Gao, D. Xia, B. Feng, M. Chen, X. He, M. Yin, Z. Xu, N. Witman, W. Fu, J. Zheng, Tissue-engineered trachea from a 3D-printed scaffold enhances whole-segment tracheal repair, *Sci. Rep.* 7 (1) (2017) 5246, <https://doi.org/10.1038/s41598-017-05518-3>.
- [45] R. Di Gesù, A.P. Acharya, I. Jacobs, R. Gottardi, 3D printing for tissue engineering in otolaryngology, *Connect. Tissue Res* 61 (2) (2020) 117–136, <https://doi.org/10.1080/03008207.2019.1663837>.
- [46] S. Dharmadhikari, L. Liu, K. Shontz, M. Wiet, A. White, A. Goins, H. Akula, J. Johnson, S.D. Reynolds, C.K. Breuer, T. Chiang, Deconstructing tissue engineered trachea: assessing the role of synthetic scaffolds, segmental replacement and cell seeding on graft performance, *Acta Biomater.* 102 (2020) 181–191, <https://doi.org/10.1016/j.actbio.2019.11.008>.
- [47] F. Sun, Z. Shen, B. Zhang, Y. Lu, Y. Shan, Q. Wu, L. Yuan, J. Zhu, S. Pan, Z. Wang, C. Wu, G. Zhang, W. Yang, X. Xu, H. Shi, Biomimetic in situ tracheal microvascularization for segmental tracheal reconstruction in one-step, *Bioeng. Transl. Med.* 8 (4) (2023), e10534, <https://doi.org/10.1002/btm2.10534>.